The Astrophysical Journal, 826:203 (14pp), 2016 August 1 doi:10.3847/0004-637X/826/2/203

STUDIES OF THE ORIGIN OF HIGH-FREQUENCY QUASI-PERIODIC OSCILLATIONS OF MASS-ACCRETING BLACK HOLES IN X-RAY BINARIES WITH NEXT-GENERATION X-RAY TELESCOPES

Banafsheh Beheshtipour, Janie K. Hoormann, and Henric Krawczynski
Physics Department and McDonnell Center for the Space Sciences, Washington University in St. Louis, One Brookings Drive, CB 1105, St. Louis, MO 63130, USA; b.beheshtipour@wustl.edu
Received 2015 September 22; revised 2016 May 17; accepted 2016 May 28; published 2016 August 1

ABSTRACT

Observations with *RXTE* (*Rossi X-ray Timing Explorer*) revealed the presence of high-frequency quasi-periodic oscillations (HFQPOs) of the X-ray flux from several accreting stellar-mass black holes. HFQPOs (and their counterparts at lower frequencies) may allow us to study general relativity in the regime of strong gravity. However, the observational evidence today does not yet allow us to distinguish between different HFQPO models. In this paper we use a general-relativistic ray-tracing code to investigate X-ray timing spectroscopy and polarization properties of HFQPOs in the orbiting Hotspot model. We study observational signatures for the particular case of the 166 Hz quasi-periodic oscillation (QPO) in the galactic binary GRS 1915+105. We conclude with a discussion of the observability of spectral signatures with a timing-spectroscopy experiment such as the *LOFT* (*Large Observatory for X-ray Timing*) and polarization signatures with space-borne X-ray polarimeters such as *IXPE* (*Imaging X-ray Polarimetry Explorer*), *PolSTAR* (*Polarization Spectroscopic Telescope Array*), *PRAXyS* (*Polarimetry of Relativistic X-ray Sources*), or *XIPE* (*X-ray Imaging Polarimetry Explorer*). A mission with high count rate such as *LOFT* would make it possible to get a QPO phase for each photon, enabling the study of the QPO-phase-resolved spectral shape and the correlation between this and the flux level. Owing to the short periods of the HFQPOs, first-generation X-ray polarimeters would not be able to assign a QPO phase to each photon. The study of QPO-phase-resolved polarization energy spectra would thus require simultaneous observations with a first-generation X-ray polarimeter and a *LOFT*-type mission.

Key words: accretion, accretion disks – black hole physics – polarization – X-rays: binaries

1. INTRODUCTION

The X-ray observations of accreting neutron stars and black holes (BHs) of the last decade and a half have revealed new avenues for testing general relativity (GR) in the regime of strong gravity (Schnittman & Bertschinger 2004; Psaltis 2008). The *Rossi X-ray Timing Explorer* (*RXTE*) revealed high-frequency (>40 Hz) quasi-periodic oscillations (QPOs) in a number of accreting BHs in X-ray binaries (Remillard & McClintock 2006). Altogether, high-frequency QPOs (HFQPOs) have been found in seven systems, three with a detection at a single frequency, and four with a detection at multiple frequencies. The binaries GRO J1655-40 and possibly also GRS1915+105 exhibit pairs of HFQPOs with frequencies in the ratio 3:2 (Remillard & McClintock 2006). QPOs may become a powerful tool for the study of BHs, i.e., to inform us about the emission state, the BH spin, and/or to test GR in the regime of strong gravity.

A number of models have been developed to explain the observed QPOs in different frequency ranges. Stella & Vietri (1998) explain the HFQPOs in low-mass X-ray binaries as the general-relativistic Lense–Thirring precession of the innermost disk region. Abramowicz & Kluźniak (2001) explain HFQPOs as a resonance of the orbital and epicyclic motion of the accreting matter. Bursa (2005) shows that the resonance between the vertical epicyclic frequency and the periastron precession frequency gives for the source GRO J1655-40 a spin estimate that is consistent with that from the X-ray continuum method. The torus model, first presented by Rezzolla et al. (2003), posits that p-mode oscillations of an accretion torus cause the HFQPOs. Bursa et al. (2004) study the flux variability induced by radial oscillations of the torus for a Schwarzschild BH. Their calculations indicate that the high-frequency modulation of the X-ray flux could result from light bending in the strongly curved BH spacetime (causing high-frequency flux variations). The resonance model of Petri (2008) explains HFQPOs as resulting from the resonance of a spiral wave in the inner part of the accretion disk with vertical epicyclic oscillations. Recently, Dexter & Blaes (2014) proposed that the local and vertical epicyclic and acoustic breathing modes could lead to HFQPOs being observed in the spectral state with a steep power law. Wagoner et al. (2001) and Kato (2003) also explain HFQPOs with the adiabatic perturbations of the relativistic accretion disk. Last but not least, Tagger & Varniere (2006) and Fukumura & Kazanas (2008) explain the HFQPOs as the observational signature of magnetohydrodynamic Rossby wave instabilities and as the light echo, respectively.

In this paper we study observational signatures predicted by the hotspot (HS) model (Schnittman & Bertschinger 2004). This model assumes an accretion disk with a bright HS orbiting the BH. The model is motivated by the similarity between the HFQPO and the coordinate frequency near the innermost stable circular orbit (ISCO). Furthermore, following the work of Merloni et al. (1999), the resonance between azimuthal and radial oscillations may explain the observed integer commensurabilities between different HFQPO frequencies (Schnittman & Bertschinger 2004). Also, recently Li & Bambi (2014) argued that the HS model can distinguish BHs and wormholes based on infrared observations.

In this paper we study the spectral and spectropolarimetric observational signatures of the HS model. A timing and spectroscopy mission such as the *Large Observatory for X-ray Timing* (*LOFT*) is ideally suited to detecting HFQPOs (Feroci et al. 2012; Vincent et al. 2013; Bozzo et al. 2014) and to

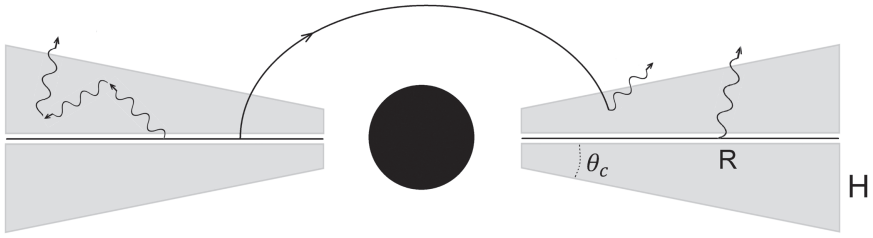

Figure 1. Sketch of a wedge corona geometry and some possible photon paths. The corona extends above and below the accretion disk with a constant opening angle, $\tan(\theta_c) = H/R$. Photons may reach the observer directly or scatter once or multiple times in the corona and/or off the disk. The strong gravitational field also deflects the photon paths.

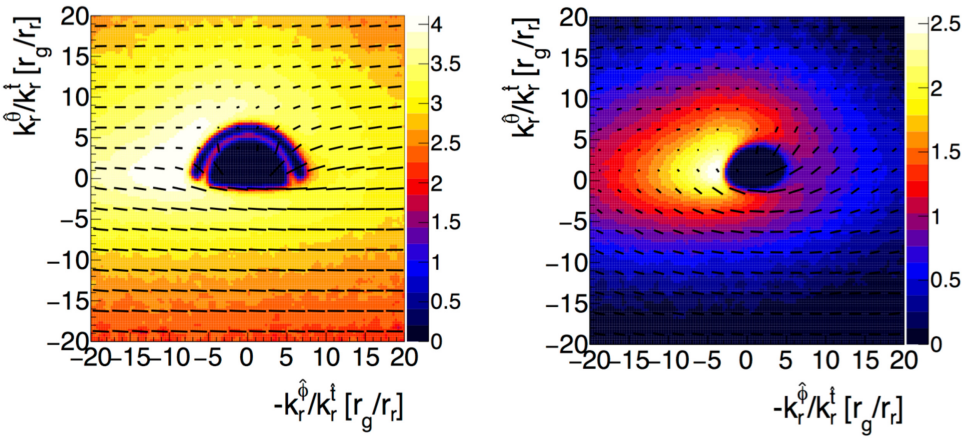

Figure 2. Image of the steady emission from the accretion disk of a Schwarzschild BH ($a = 0$ and $M = 10\ M_\odot$) at an inclination of 75° (left panel), and GRS 1915+105 ($a = 0.95$ and $M = 14\ M_\odot$) at an inclination of 66° (right panel). The observed intensity is color-coded on a logarithmic scale. The length and orientation of each bar show the polarization fraction and polarization angle, respectively. We measure the polarization angle from the projection of the spin axis of the BH in the plane of the sky, and it increases for a clockwise rotation when looking toward the BH.

measuring phase-resolved energy spectra of QPOs. Spectroscopic X-ray polarimetry observations (see, e.g., Meszaros et al. 1988; Lei et al. 1997; Li et al. 2009; Schnittman & Krolik 2009; Bellazini et al. 2010; Krawczynski 2012), offering three times as much information as purely spectroscopic observations (i.e., the Stokes parameters I, Q, and U rather than I alone as functions of energy), would offer additional handles to distinguish between HFQPO models. As some X-rays scatter before leaving the accretion disk, even the thermal emission is polarized (e.g., Li et al. 2009 and references therein). The polarization angle changes as the X-rays propagate through the strongly curved spacetime of the BH. Additional photon scattering off the accretion disk or in its corona modifies the polarization fraction and angle. Zamaninasab et al. (2010, 2011) studied the polarization of HSs orbiting supermassive BHs at infrared wavelengths and used infrared observations of the supermassive BH Sgr A* to constrain its mass and spin.

We use the ray-tracing code developed by Krawczynski (2012) to model the X-ray emission from HSs orbiting Schwarzschild and Kerr stellar-mass BHs in X-ray binaries. Although our studies are generic in nature, our Kerr BH calculations adopt parameters chosen to describe the 166 Hz QPO of the galactic BH GRS 1915+105. HFQPOs have been observed in the steep power-law (SPL) state of BHs. The SPL state is commonly attributed to a corona of hotter gas that reprocesses the photons from the accretion disk and gives rise to a power-law emission spectrum (e.g., Remillard & McClintock 2006). Since the geometry and physical properties of a corona are not fully understood, a wide range of coronal models have been proposed (e.g., Haardt & Maraschi 1991;

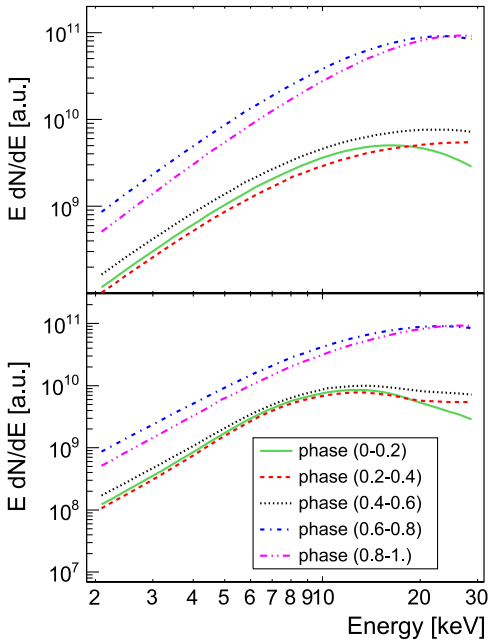

Figure 3. Phase-resolved energy spectra of a HS orbiting GRS 1915+105 for HS emission (upper panel) and total emission (lower panel).

Dove et al. 1997; Nowak et al. 2002; McClintock & Remillard 2003; Schnittman & Krolik 2010). In this paper we model a geometrically thin, optically thick accretion disk with an orbiting HS with and without a sandwich corona. The corona's

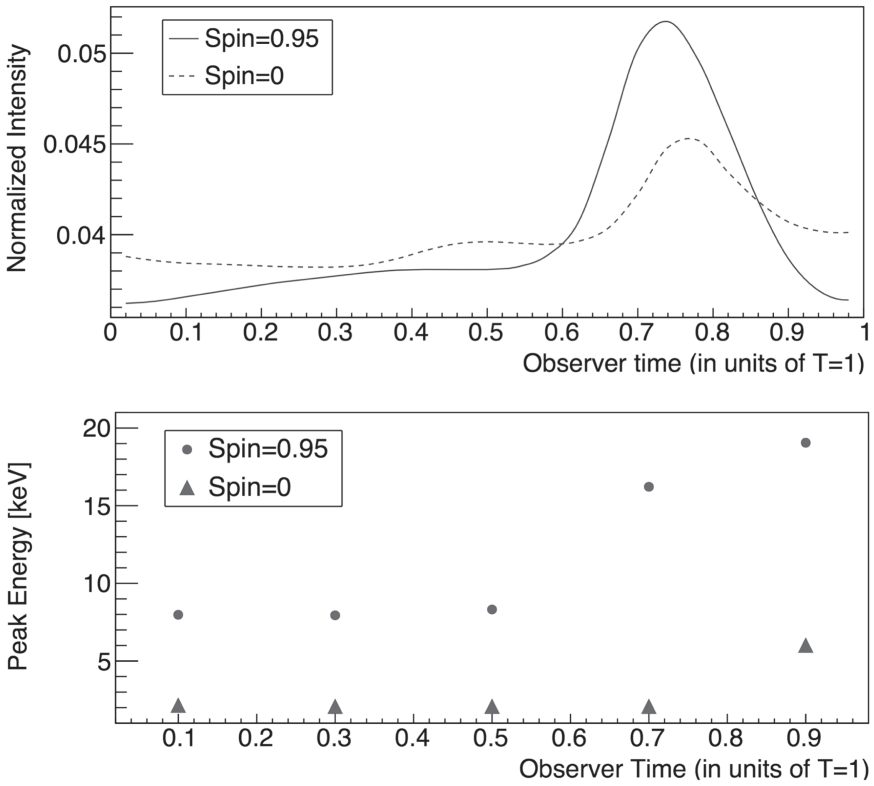

Figure 4. Intensity (i.e., average 2–30 keV photon flux) (upper panel) and peak energy (lower panel) of the total X-ray emission from the Schwarzschild and Kerr BHs. The intensity is normalized to 1 when integrated over all phases.

properties have been chosen to give the power-law energy spectrum of GRS 1915+105 in the SPL state.

In a somewhat related study Ingram et al. (2015) have studied the polarization properties of *low-frequency QPOs* assuming that they originate from the Lense–Thirring precession of the inner accreting flow. They find variations in the polarization fraction of the order of 1%, which could be detected and studied by an X-ray polarimeter with hard X-ray sensitivity such as the proposed *Polarization Spectroscopic Telescope Array* (*PolSTAR*) mission.

The rest of the paper is structured as follows. We summarize the HS model and describe our simulations in Section 2. Section 3 presents the results for Schwarzschild and Kerr BHs, including a discussion of the observational signatures as a function of the HS parameters. In Section 4 we summarize the results and discuss the expected energy spectra and polarization signatures of competing HS models. Throughout this paper, all distances are in units of gravitational radius $r_g = GM/c^2$, and we set $G = c = \hbar = 1$.

2. METHODOLOGY

2.1. The Hotspot Model

Stella & Vietri (1998, 1999) introduced the HS model to explain the observations of QPOs with frequencies comparable to the orbital frequencies of matter orbiting BHs and neutron stars close to the ISCO. As mentioned above, the HS can explain not only the detection of a HFQPO at one frequency but also twin HFQPOs with integer frequency ratios as the result of nonlinear resonances occurring near geodesic orbits (Abramowicz & Kluźniak 2001, 2003).

The HS model posits that a region with a temperature exceeding that of the ambient material orbits the BH. We assume that all the matter orbits the BH on a nearly circular orbit with the angular frequency ν_ϕ given by Bardeen et al. (1972):

$$\Omega_\phi = 2\pi\nu_\phi = \frac{\pm\sqrt{M}}{r^{3/2} \pm a\sqrt{M}}. \quad (1)$$

The upper (lower) sign applies for a prograde (retrograde) orbit. Typically, we consider HSs with a radius of around 0.25–0.5 r_g. It has been argued that a larger HS will not survive a long time because of the viscous shearing of the disk (Markovic & Lamb 2000). Schnittman & Bertschinger (2004) have shown that the light curve and the HFQPO power spectrum are independent of the HS's size and shape. They also tried to explain the 3:2 commensurability for twin peaks in some X-ray binary systems with the idea of a noncircular orbit of the HS and its different coordinate frequencies. These properties lead to some beat frequency in the light curve and the authors believe that one of the peaks is at the azimuthal frequency and the other is at beat modes $\nu_\phi \pm \nu_r$.

Schnittman (2005) modeled HFQPOs with a couple of orbiting HSs, assuming a random phase, different lifetimes, and a finite width for HSs. The model produced broad HFQPOs with Q-factors—defined as the ratios of the HFQPO line centroids to the linewidths (FWHM)—matching the observed ones.

We neglect the Faraday rotation that polarized photons would experience in a magnetized plasma, an assumption that seems to hold at photon energies exceeding a few keV (Davis et al. 2009).

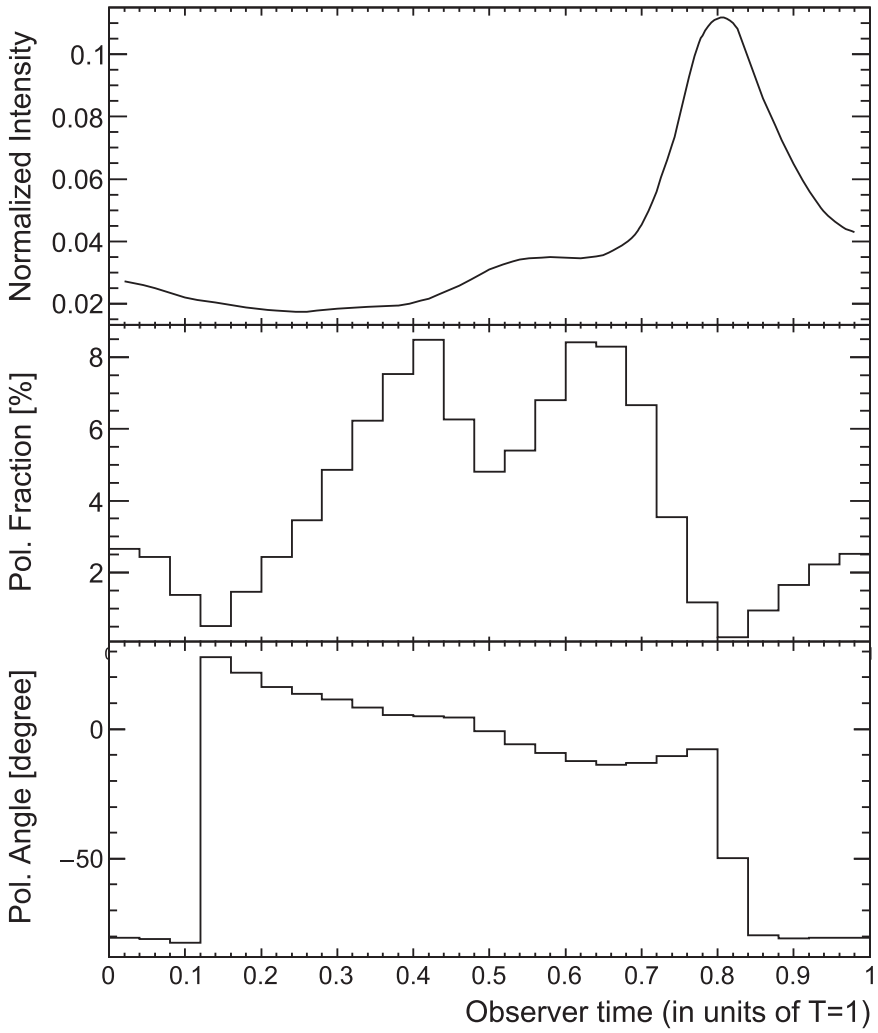

Figure 5. Intensity, polarization fraction, and polarization angle of the HS emission for a Schwarzschild BH, viewed at an inclination of 75°. The emission is polarized with a maximum polarization fraction of ≈8.5%. The polarization angle exhibits a full 180° swing in one orbit. A polarization angle of 0° corresponds to emission with an electric field vector perpendicular to the spin axis of the accretion disk.

2.2. Thermal Disk Simulation

We assume that the HS is a disk segment emitting with a temperature five times higher than the surrounding material. This temperature gives (for the adopted HS size) HFQPO rms amplitudes comparable to the observed ones. The effects of the HS size on the observable signatures are discussed in the Section 3. The HS of the Schwarzschild BH extends from the ISCO ($r_{\rm ISCO} = 6$) to $r = r_{\rm ISCO} + 2\Delta r$, where $\Delta r = 0.5$ and from ϕ to $\phi + \Delta\phi$, where $\Delta\phi = 0.08\pi$. The HS of the Kerr BH is centered at the radial coordinate $r = 5 + \Delta r$ to model the 166 Hz QPO of GRS 1915+105.

We use the general-relativistic ray-tracing code of Krawczynski (2012). Photons are tracked forward in time from their emission site to the observer, including, if applicable, one or several scatterings off the accretion disk. The standard Novikov–Thorne radial brightness profile of a geometrically thin, optically thick accretion disk is used to weigh the simulated rays (Novikov & Thorne 1973; Page & Thorne 1974). Recent general-relativistic magnetohydrodynamic (GRMHD) simulations show that the Novikov–Thorne results are a good approximation to the more detailed results (Noble et al. 2009; Penna et al. 2010, 2012).

The code simulates an accretion disk extending from $r_{\rm ISCO}$ to $r_{\rm max} = 100\ r_{\rm g}$. For each background metric, we divide the accretion disk into 10,000 radial bins spaced equally in the logarithm of the Boyer–Lindquist coordinate r. For each radial bin, we simulate 1000 photon packages. For the radially symmetric emission from the accretion disk, the code makes use of the azimuthal symmetry of the problem: all photons are launched at an azimuthal angle $\phi = 0$. When they leave the simulation sphere, we infer that the probability of finding them in the azimuth angle interval from ϕ to $\phi + \Delta\phi$ is equal to $\Delta\phi/2\pi$. Photons are created in the plasma frame with a limb-darkening function from Chandrasekhar (1960). The code uses Table XXIV of Chandrasekhar (1960) to calculate the initial polarization of the photon and the statistical weight for its direction of emission. Subsequently, the photon wavevector and polarization vector are transformed into the Boyer–Lindquist frame. The photons are then tracked by solving the geodesic equation:

$$\frac{d^2x^\mu}{d\lambda'^2} = -\Gamma^\mu{}_{\sigma\nu}\frac{dx^\sigma}{d\lambda'}\frac{dx^\nu}{d\lambda'}, \tag{2}$$

with λ' being an affine parameter and $\Gamma^\mu_{\sigma\nu}$ the Christoffel symbols. The polarization vector is parallel transported with the

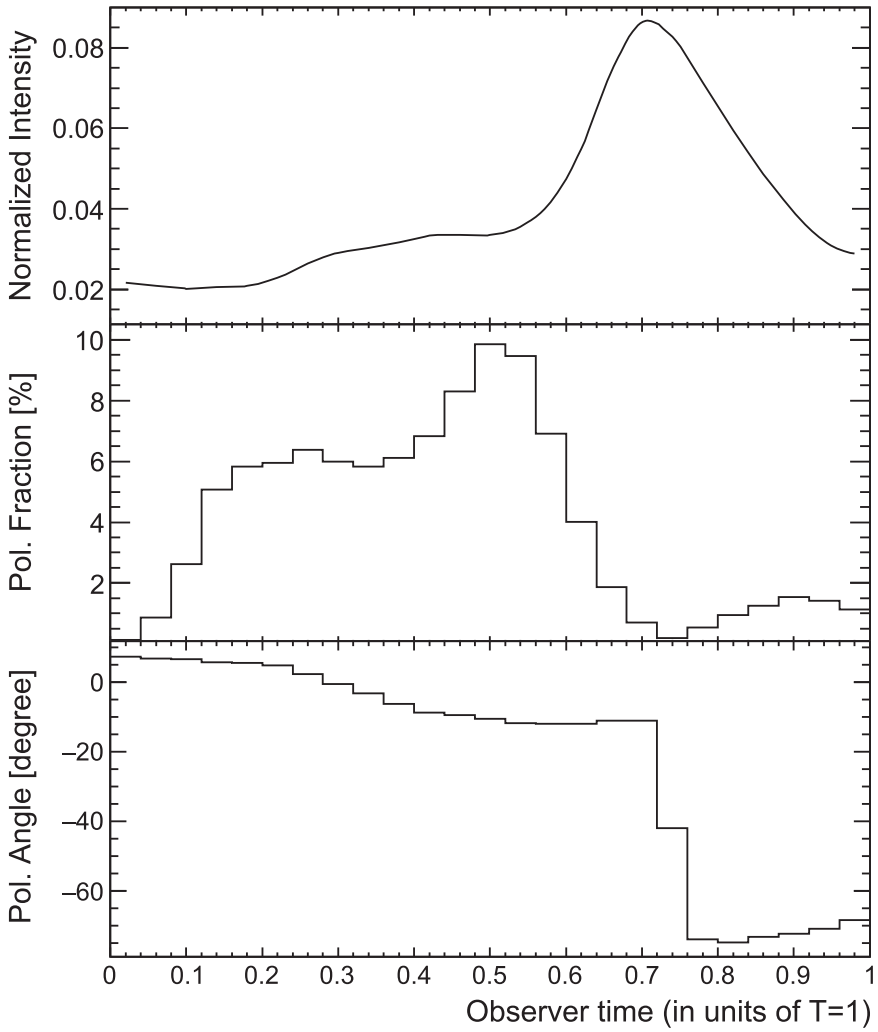

Figure 6. The same as Figure 5 for a HS orbiting the Kerr BH. The emission is highly polarized with a maximum polarization fraction of ≈10%. The polarization angle swings by 90° during one orbit.

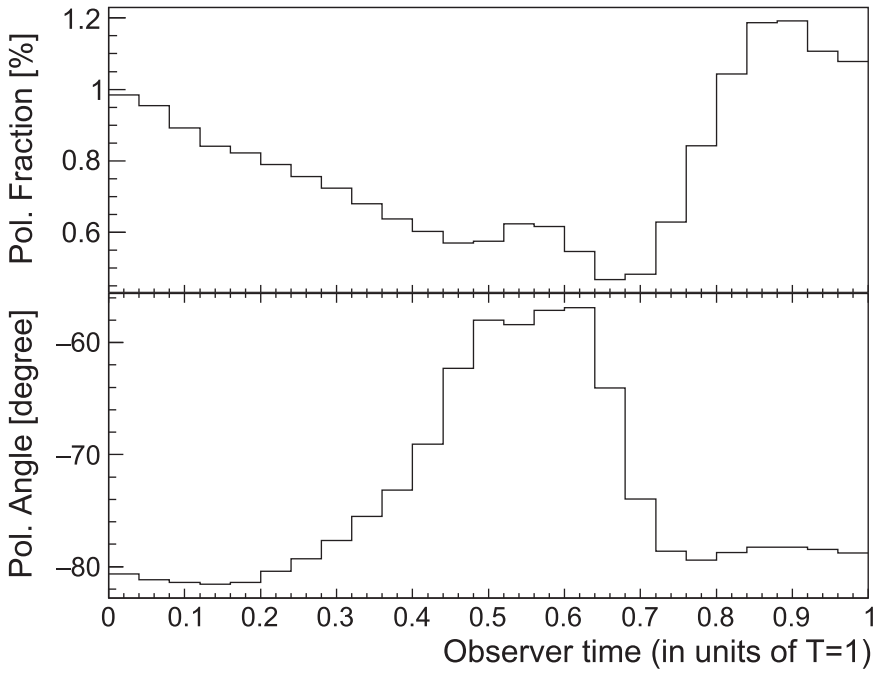

Figure 7. Polarization fraction and angle of the HS plus disk emission for the Kerr BH. This is polarized with a maximum polarization fraction of ≈1.2%.

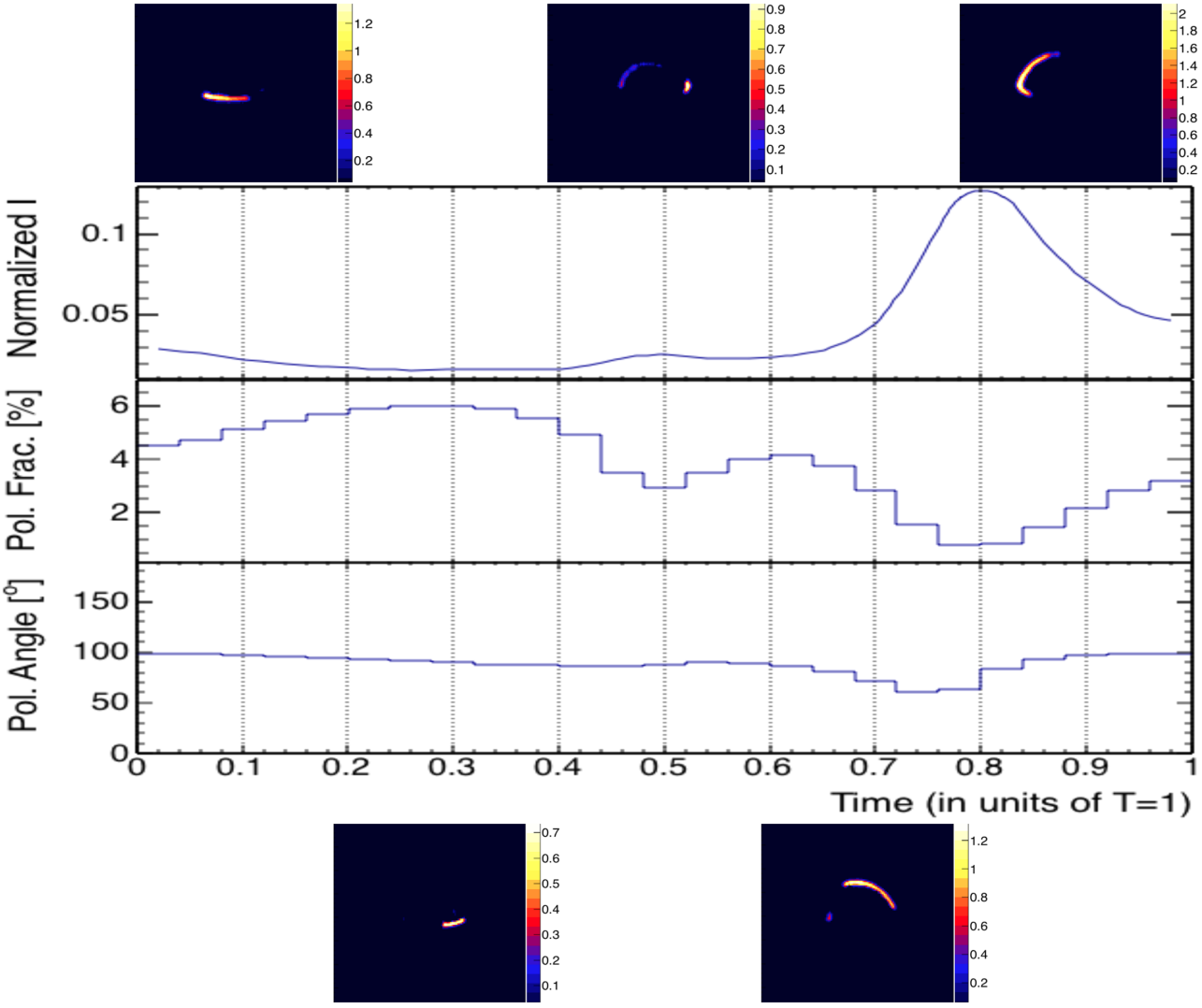

Figure 8. Light curve, polarization fraction, and angle, and images of the direct emission from a HS orbiting the Schwarzschild BH viewed at 75° inclination (relative to the spin axis of the accretion disk). The images show the HS in five phase bins. For instance, the first image (top left) shows the emission of the phase bin from $t = 0$ to $t = 0.2\,T$, T being the HS period. The axis label and scale for the images are the same as in Figure 2. The intensity is normalized to 1 when integrated over all phases.

equation

$$\frac{df^{\mu}}{d\lambda'} = -\Gamma^{\mu}{}_{\sigma\nu} f^{\sigma} \frac{dx^{\nu}}{d\lambda'}. \tag{3}$$

At the analysis stage, the photon packages are weighted to mimic the radial brightness distribution $F(r)$ of Page & Thorne (1974). The latter authors used the conservation of mass, angular momentum, and energy to derive

$$F(r) = \frac{-\dot{M}}{4\pi} e^{-(\nu+\psi+\mu)} \frac{p^{t}_{,r}}{p_{\phi}} \int_{r_{\rm ISCO}}^{r} \frac{p_{\phi,r}}{p^{t}} dr \tag{4}$$

where $\dot{M}$ is the accretion rate for a stationary, axially symmetric metric given by the functions ν, ψ, and μ, and p^{μ} is the four-momentum of the disk material with "," denoting ordinary partial differentiation (see Bardeen et al. 1972 and Page & Thorne 1974 for the nomenclature). Photon packages are assumed to be emitted with a blackbody energy spectrum with the temperature

$$T_{\rm eff} = \left(\frac{F(r)}{\sigma_{\rm SB}}\right)^{\frac{1}{4}}. \tag{5}$$

The code tracks the red- and blueshifts of the photons between emission and absorption (including the gravitational redshifts and blueshifts incurred during propagation), and the thermal energy spectrum is then red- or blueshifted when accounting for the detected photon packages. The HS is treated in the same way, except that the effective temperature and thus the brightness and the statistical weight are higher for this segment. For simplicity we do not reduce the temperature of the adjacent parts of the accretion disk, which would be required in a self-consistent steady-state solution. The slight reduction in temperature of the adjacent material would enlarge the contrast between the HS and the disk and would thus enlarge the observational signatures.

When a photon hits the accretion disk, it is scattered into a random direction with equal probability in solid angle and with

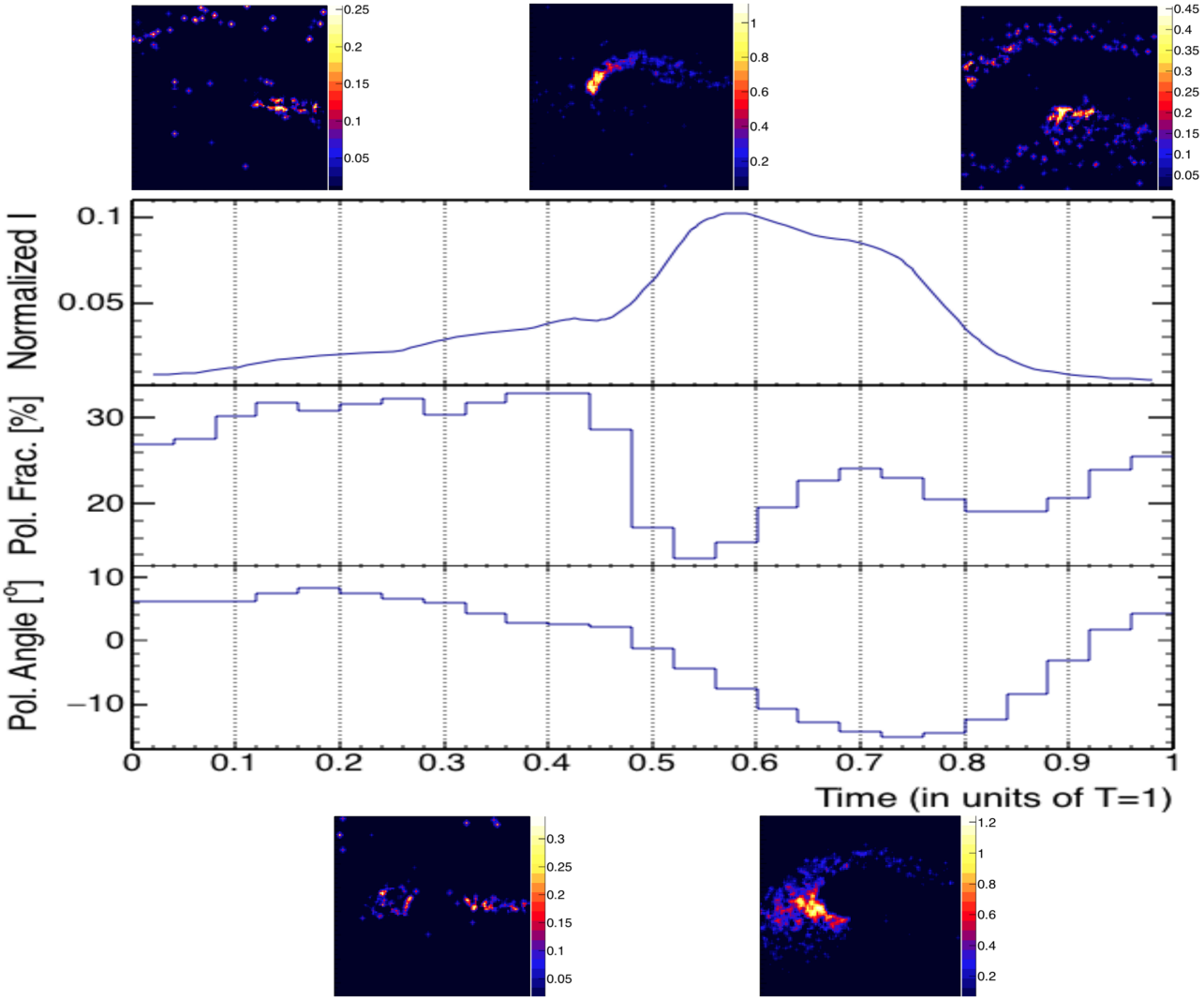

Figure 9. The same as Figure 8 for the emission returning to the accretion disk and being scattered at least once.

a statistical weight determined from Table XXIV of Chandrasekhar (1960). The photon is tracked until it comes too close to the event horizon ($r < r_H + 0.02$), or until its radial Boyer–Lindquist coordinate r exceeds 10,000 r_g. If the latter happens, the photon is backtracked to $r = 10{,}000$. Subsequently, its wave vector and polarization vector are transformed into the reference frame of an observer at fixed coordinates. These results, together with the information about the degree of polarization (a Lorentz invariant) are then used to determine the photon energy and the Stokes parameters I, Q, and U of all photons detected in a certain range of polar angle. In the final step, the Stokes parameters are used to find the polarization fraction and angle of each photon. The interested reader can find a more detailed description of the ray-tracing code in Krawczynski (2012).

2.3. Corona Simulation

We simulate a simple corona geometry, an isothermal layer with a constant opening angle forming a wedge above and below the accretion disk (see Figure 1). The vertical optical depth of this layer is set to a constant, $\tau_0 = 0.2$, and the temperature of the hot electrons in the corona is set to $T_{\rm corona} = 30$ keV. These parameters reproduce the observed photon index for GRS 1915+105 in the SPL state (Belloni et al. 2006). The opening angle of the wedge is set to 2°. A larger opening angle would result in longer light travel times inside the corona and in a wider X-ray pulse from the HS. We assume that the corona gas orbits the BH with the angular velocity of an observer having zero angular momentum (Bardeen et al. 1972). As we track individual photons originating from the accretion disk, we check for each integration step whether the photon is inside the corona. If so, we transform the start and end points of the integration step into the rest frame of the corona plasma, and determine the optical depth between these two points. The optical depth is then used to determine the probability for Thomson scattering. We have implemented the scattering in both the Thomson and the Klein–Nishina regimes, but we use here the algorithm for Thomson scatterings (see the discussion of Schnittman & Krolik 2010 for a justification). We then draw a random direction of the scattering electron in the comoving plasma rest frame, transform the wave vector of the photon from the plasma rest frame into the rest frame of the electron, and determine the photon wave vector after scattering. Subsequently, the photon wave vector is first transformed back into the rest frame of the corona, and subsequently into the global

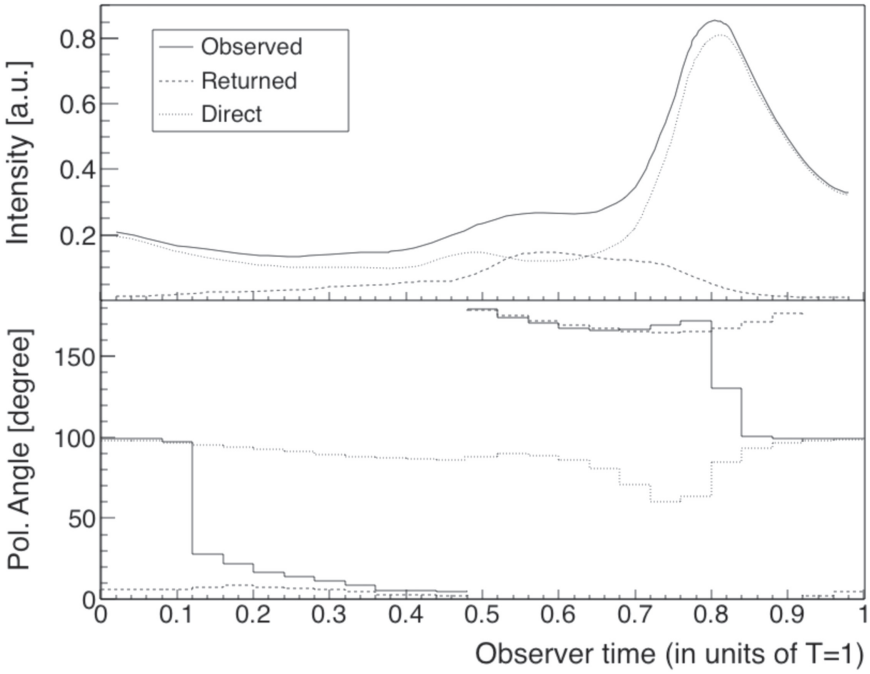

Figure 10. Intensity and polarization angle of the direct and the returning radiation, and the sum of these (observed). The results show that the polarization angle is dominated by the returning radiation for the central phase bins.

Boyer–Lindquist coordinates. A more detailed description of the modeling of the Comptonization of the photons in the corona will be given in a companion paper (B. Beheshtipour et al. 2016, in preparation).

3. RESULTS

In the following, all results will be given for the 2–30 keV energy band unless otherwise specified. The inclination is $i = 0°$ for an observer viewing the disk face-on and $i = 90°$ for an observer viewing the disk edge-on. In all light curves (intensity plots) we give the average 2–30 keV photon flux.

3.1. Thermal Emission

Figure 2 shows an accreting Schwarzschild BH at an inclination of 75°, and the accreting Kerr BH (GRS 1915+105) seen at an inclination of 66° (Fender et al. 1999) for the 2–15 keV energy band. The lengths and orientations of the bars in the image show the polarization fractions and angles, respectively. The image clearly shows the relativistic beaming and de-beaming of the emission from the disk, resulting in pronounced brightness variations across the disk (see also Schnittman & Krolik 2009).

We plot the phase-resolved energy spectra of the accretion disk and HS emission of the GRS 1915+105 model in Figure 3. We divided the orbit into five phase bins and each line in the figure shows the energy spectrum of the HS for the specific phase bin. Note that the phase also characterizes the azimuthal position of the HS. At phase = 0 (0.5) the HS is closest to (furthest away from) the observer. The energy spectra exhibit well defined flux peaks. The energies corresponding to these peaks, i.e., peak energies, for the total emission (HS plus accretion disk) are shown in Figure 4 as a function of phase for both simulated BHs. The peak energies are higher for the Kerr BH because its HS is closer to the BH (the HS center is at 5.5 r_g for the Kerr BH and 6.5 r_g for the Schwarzschild BH), allowing for bright emission from the inner regions of the accretion disk. The integral flux (i.e., intensity) drops in the last phase bin even though the energy spectrum still hardens (Figure 3), owing to the Doppler shift from the relativistic motion of the accretion disk plasma. This can be understood as follows. Photons returning to the disk and scattering off the disk have a very broad energy spectrum owing to the energy gains/losses incurred during the scattering process. These scattered photons arrive a bit later than the unscattered photons, giving rise to the hard spectrum at the end of the peak. Interestingly, the flux peak leads the peak of the spectral hardness by ~0.2 in phase.

Figures 5 and 6 show the normalized intensity, polarization fraction, and angle for the Schwarzschild and Kerr BHs. The intensity is normalized to 1 when integrated over all phases. Comparing these figures, one can see the effect of the BH spin on the polarization of the observed emission. Interestingly, the HS model predicts that the peak of the emission (dominated by direct HS emission relativistically beamed toward the observer) is accompanied by a drop in polarization fraction and a large swing of the polarization direction. As shown below, the polarization properties result from the competition of the direct HS emission and the HS emission reflecting off the accretion disk. Also, the effect of including the emission of both the disk and the HS on the polarization fraction and angle is shown in Figure 7. The total polarization is lower due to the disk emission being less polarized.

Figures 8 and 9 show (for the Schwarzschild BH) the light curve and polarization angle of an orbiting HS together with snapshot images of the emission made with direct (unscattered photons) and returning (scattered photons) radiation, respectively. In the top middle snapshot in Figure 8 the bottom ring is observable due to the extreme curvature of the spacetime close to the BH. The light curve in Figure 8 demonstrates that the HS is brightest in the 0.7 T–0.9 T phase bin (with T being the orbital period of the HS). The apparent brightness distribution results from the combined effects of relativistic boosting and

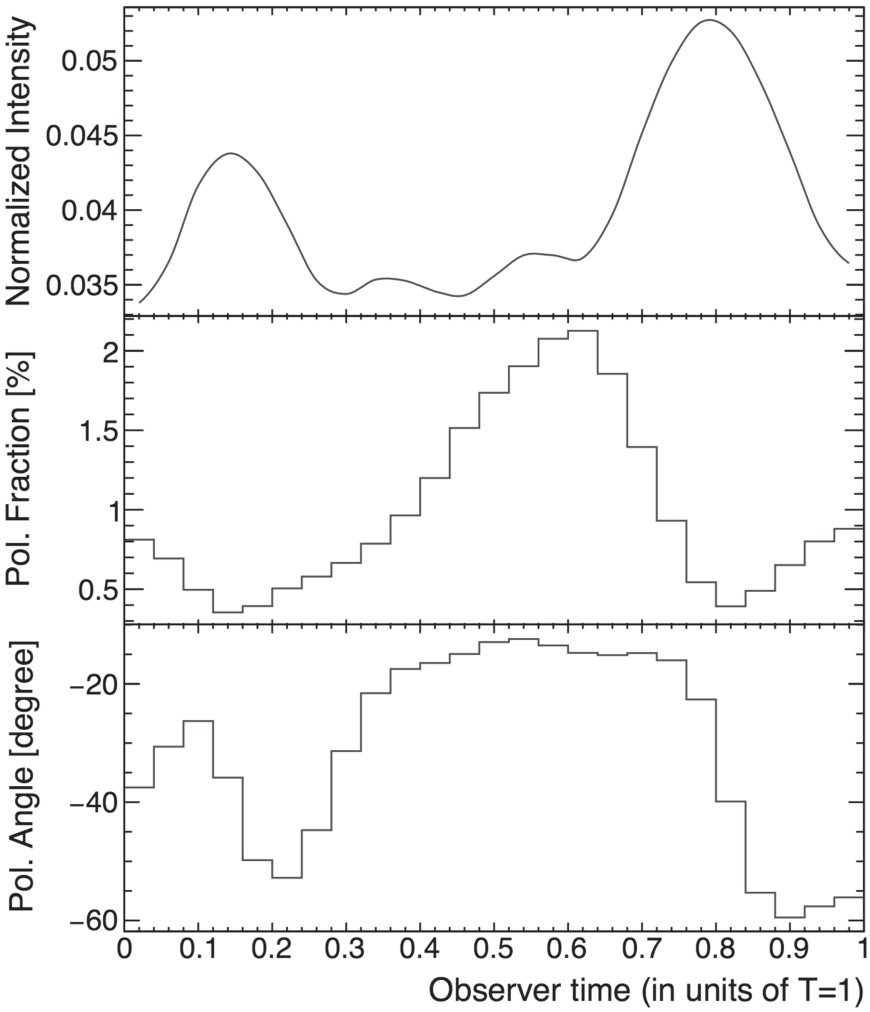

Figure 11. Intensity, polarization fraction, and polarization angle of the emission from 10 identical HSs for the Kerr BH, viewed at an inclination of 66°. The emission is polarized with a maximum polarization fraction of ≈2.2%.

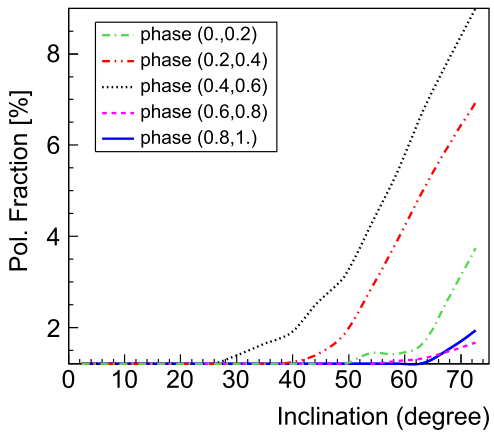

Figure 12. Polarization fraction versus inclination for GRS 1915+105. Different lines show different phase bins. The polarization fractions increase with increasing inclination.

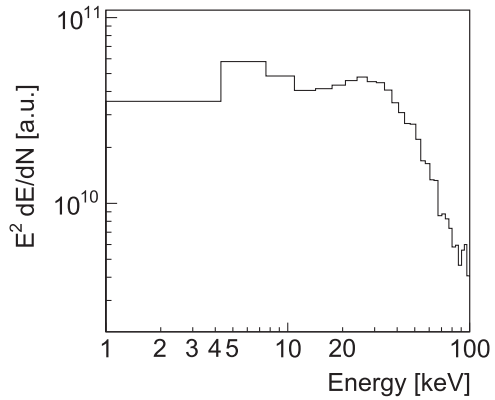

Figure 13. Observed energy flux per logarithmic energy interval $E^2\ dN/dE$ from the accretion disk with a sandwich geometry for GRS 1915+105. The Comptonized spectrum has a photon index of ≈2.7.

light travel time. The spot appears to orbit faster during the first half of its orbit. The same result is seen for GRS 1915+105.

The polarization angle in Figures 8 and 9 shows how it is affected by scattering. Approximately between 10% and 40% of photons scatter off the disk, depending on the phase of the HS. These scattered photons are highly polarized and thus strongly impact the net polarization of the signal (Figure 9). The influence of the scattered photons on the polarization angle can be seen from the intensities (Figure 10). For direct photons the polarization vector is mostly parallel (±90°). The scattered photons acquire a 90° rotated polarization angle. In the 0.1 T–0.7 T phase bin, the returning radiation intensity becomes higher, so the observed polarization angle is dominated by

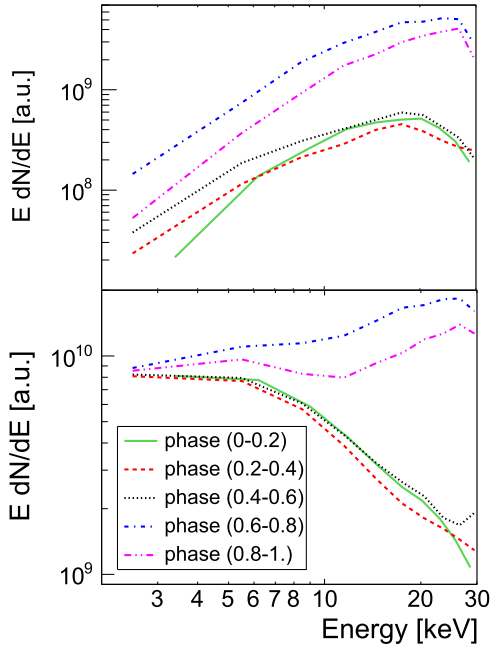

Figure 14. Phase-resolved energy spectra of a HS emission (upper panel) and total emission (lower panel) for GRS 1915+105 with a sandwich corona geometry.

returning radiation, which is strongly polarized, thus it is around $0°/180°$. For phases over $0.8\,T$ the direct intensity with a $90°$ rotated polarization angle dominates. Furthermore, the change in the polarization angle is larger for the Kerr BH than for the Schwarzschild BH owing to the stronger curved spacetime of the Kerr BH and the larger fraction of photons returning to the accretion disk for a Kerr BH with a smaller ISCO.

All polarization plots show an anticorrelation between the intensity and the polarization fraction of the HS. For example, in Figure 6, we see that the high fluxes in the second half of the orbit are polarized to a low degree. The effect is smaller for the Schwarzschild BH, which shows higher polarization fractions than the Kerr BH at the end of the orbit. The effect of photons returning to the accretion disk on the polarization fraction owing to the curved spacetime is shown in Figure 9. Not only does the figure emphasize that scattering leads to a strong polarization of the returning radiation, but it also confirms the anticorrelation of intensity and polarization fraction. The same result is seen for GRS 1915+105.

It is instructive to compare our results with those of Broderick & Loeb (2005), who modeled the polarized emission of a HS orbiting a BH. While the emission of the HSs in Figures 5 and 6 depolarizes when the intensity peaks, the HS emission of Broderick & Loeb depolarizes briefly before the intensity peaks. We explain the different results in three main ways. (i) Our code assumes that the initial polarization of the emission is given by Chandrasekhar's classical results for the emission of an optically thick atmosphere (Chandrasekhar 1960): the polarization fraction increases from zero close to the zenith to a few per cent close to the horizon (where "zenith" and "horizon" refer to an observer in the disk frame) and the polarization direction is perpendicular to the plane of the zenith and the direction of emission. In contrast, Broderick & Loeb assume a constant polarization fraction, always orthogonal to the spin axis of the BH. (ii) Whereas we model the X-ray emission returning to and scattering off the accretion disk (strongly impacting the observed net polarization), Broderick & Loeb do not do so. (iii) Broderick and Loeb assumed a different HS geometry and size, and the predicted results are to some extent dependent on them.

A single pronounced HS produces cleaner observational signatures than a combination of several HSs. We studied the observational appearance of multiple HSs by simulating an accretion disk with 10 identical HSs. We assume that the HSs orbit the BH at the same distance but with a random phase. Figure 11 shows the light curve and polarization signature of this simulation for the Kerr BH. Similar to the results for a single HS, we see that the polarization fraction anticorrelates with the flux. The variation in polarization is smaller than for a single HS in the same way as a bigger HS leads to smaller variations in polarization because the polarizations of different parts of the HS do not add up coherently.

Furthermore, we investigate the change in polarization by changing the inclination of the BH and size of the HS. Figure 12 shows that the polarization fraction increases with BH inclination. Note that in the simulation of Schnittman & Bertschinger (2004) the HFQPO amplitude exhibits a similar behavior with increasing inclination. For polarization angle, there is no simple behavior but generally it decreases with increasing inclination as a result of the lower polarization of photons leaving the emitting plasma in its reference frame closer to the surface normal. Larger HSs are less polarized than smaller HSs because averaging over different polarization directions reduces the polarization fraction. The HS polarization also gets smaller when increasing the distance of the HS from the BH because the fraction of returning radiation decreases. We see the same result for polarization angle by enlarging the HS. Our results show that the effects of inclination and HS size on the polarization are stronger for the Kerr BH than for the Schwarzschild BH. Also, in this paper we assumed that the HS temperature is $5T_{\rm eff}$ to produce the realistic modulation in flux. Whereas the polarization of the HS is independent of its temperature, the peak energy of the emission is not. A larger HS can have a lower temperature and still produce the same flux modulation. Such a larger HS would emit less polarized emission due to averaging different polarization directions over a larger area.

3.2. Coronal Emission

Figure 13 shows the power-law tail of the observed flux for the HS and coronal emission. The simulation gives a photon index close to the one observed For GRS 1915+105 by Belloni et al. (2006) in the SPL state. The phase-resolved energy spectra of the HS and the accretion disk are shown in Figure 14. The HS emission can clearly be recognized by the hard emission at the highest energies. Overall, the results look similar to those discussed in the absence of a corona (Figure 3). Figure 15 shows the normalized intensity, polarization fraction, and polarization angle for the same model. Although the polarization signatures are somewhat less pronounced when accounting for the Comptonization of the emission in the corona (because of the associated light travel delays and loss of phase information), the intensity and polarization fraction still show an anticorrelation as discussed for the model without a corona. In Figure 15 the polarization peaks around the phase $0.2\,T$, where the photons scattered in the corona are more dominant.

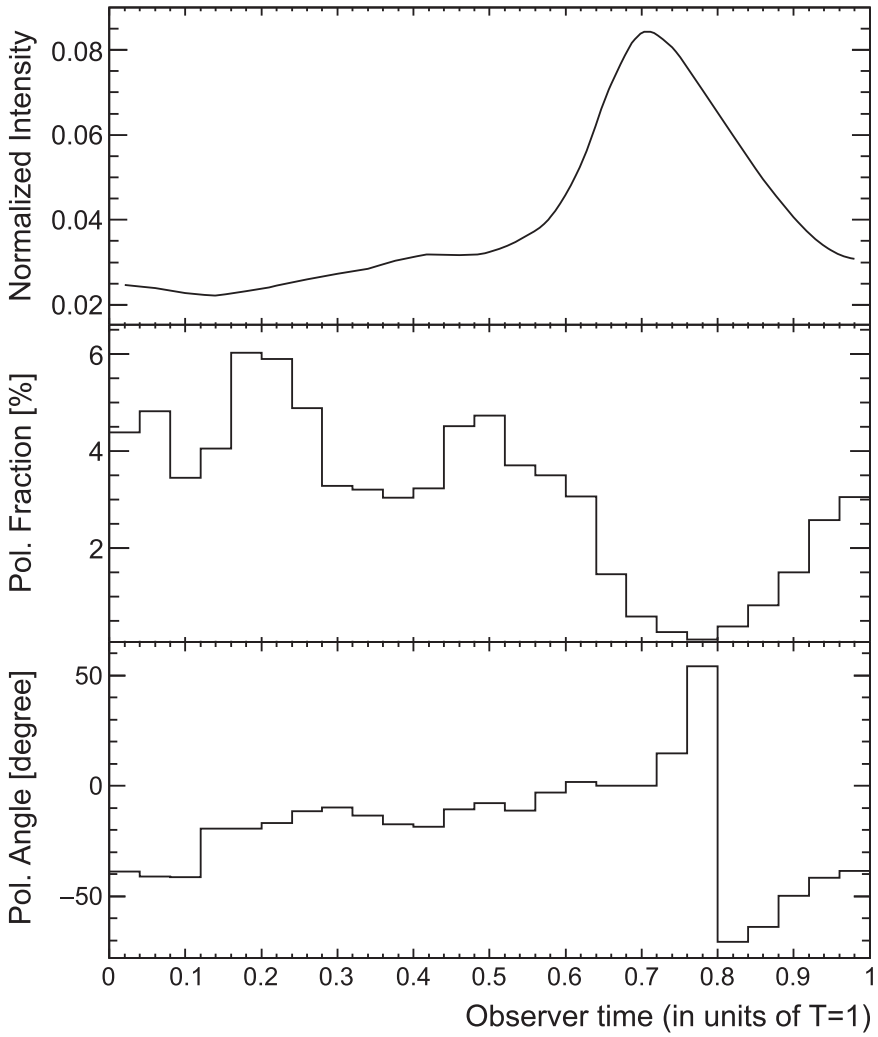

Figure 15. Intensity, polarization fraction, and polarization angle of the HS coronal emission for GRS 1915+105. The emission is polarized with a maximum polarization fraction of $\approx 6\%$.

4. SUMMARY AND DISCUSSION

This paper shows results from simulating HSs orbiting accreting Schwarzschild and Kerr BHs in X-ray binaries. The HS flux shows a pronounced peak accompanied by a hardening energy spectrum, with the hardness peak trailing the flux peak by 0.2 in phase. This specific signature could be observed by an instrument like *LOFT*. The mission would detect GRS 1915 +105 with a detection rate exceeding 100,000 counts s^{-1} (Suchy et al. 2012). Using Fourier filter techniques of Tomsick & Kaaret (2001) with the light curves with >30 detected photons during each period of the 166 Hz QPO with an rms of 6% would make it possible to determine a phase for each detected photon. The phase-resolved light curve would distinguish the HS model (predicting a sharp peak in the light curve) from competing models that predict more sinusoidal variations of the flux (see the discussion below). Phase-binning the data would make it possible to determine the peak energy of the energy spectra as a function of QPO phase as shown in Figure 4.

We carried through a detailed simulation and analysis to evaluate the detectability of the phase-resolved spectral variations with *LOFT*. We used the methods of Timmer & Koenig (1995) to simulate the time-variable emission from the accretion disk with a realistic power spectral density (Figure 16, top panel). We then used the methods of Ingram & van der Klis (2013) to simulate QPOs based on the phase-resolved HS intensity from Figure 6. Subsequently, we added statistical fluctuations to the total signal, taking the *LOFT* sensitivity into account. The bottom panel of Figure 16 shows the resulting light curve for a 1 s *LOFT* observation. Although the long-term flux evolution is dominated by the low-frequency flux variability of the accretion disk emission, the HFQPOs with a period of ≈0.006 s can clearly be recognized. Subsequently, we applied the frequency filtering method of Tomsick & Kaaret (2001), selecting on frequencies within ±20% of the HFQPO. The filtered light curve is shown in Figure 17. The filtered flux curve is subsequently used to determine the *reconstructed phase*. We find that the difference between the reconstructed and true phases is approximately normally distributed with a sigma of ≈0.08 for a 5 minutes observation of *LOFT*. The phase tagging becomes more accurate as we increase the observation time. Using the reconstructed phases, we can reconstruct phase-resolved energy spectra. The lower (upper) panel of Figure 18 shows the phase-resolved energy spectrum measured on the basis of the true (reconstructed) phase information. The phase reconstruction does reduce the differences between the phase-binned energy spectra, but not

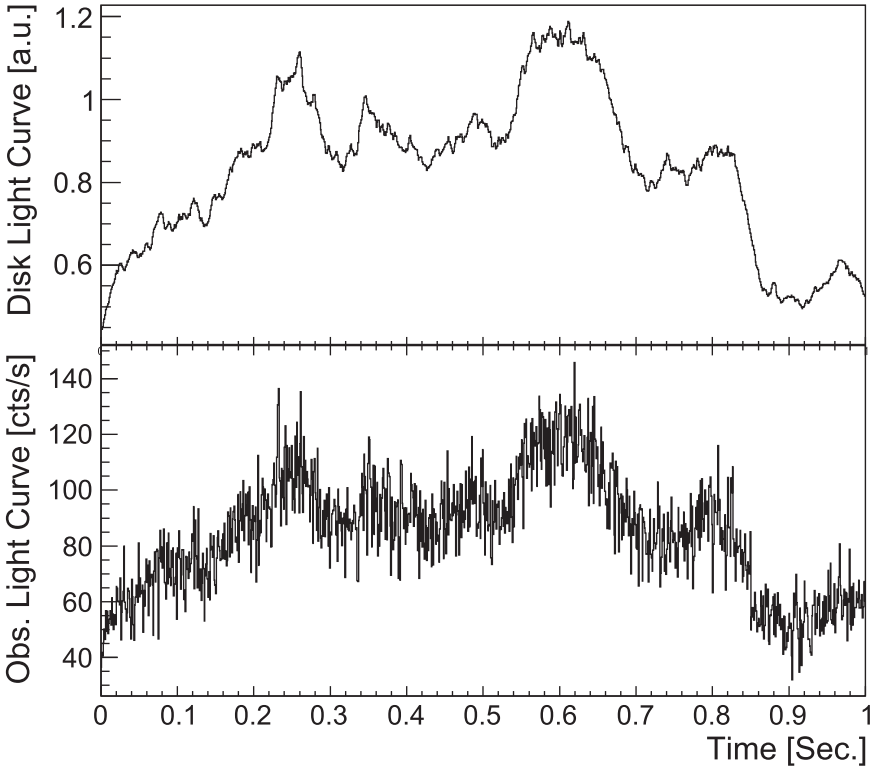

Figure 16. Examples of simulated disk emission (upper panel) and disk plus HS emission (lower panel).

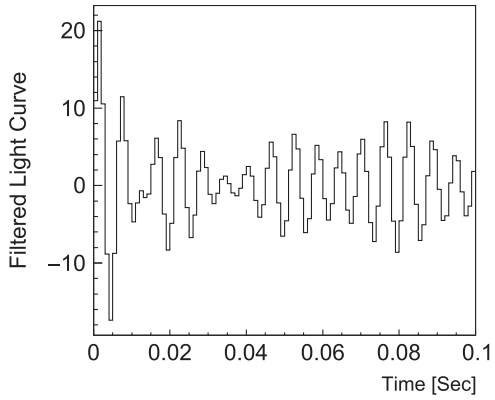

Figure 17. The observed light curve predicted for *LOFT* (Figure 16) after bandpass filtering.

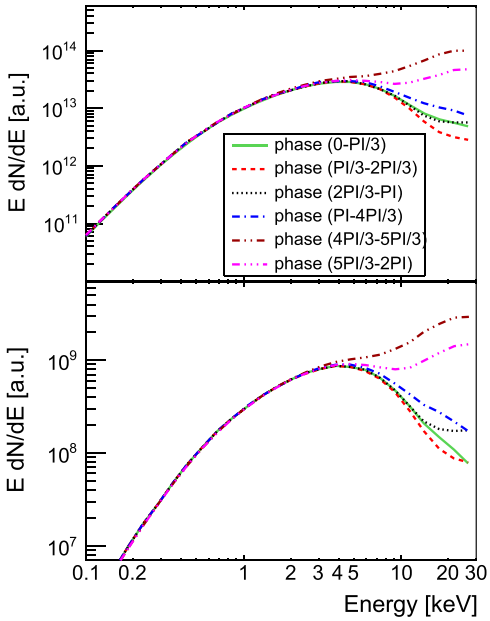

Figure 18. The folded phase-resolved energy spectra for the simulation of the *LOFT* observation (upper panel) and the phase-resolved energy spectra of the thermal model for total emission (lower panel). The orbital period is divided into six equally spaced bins, each line representing the energy spectrum observed in one of these bins.

catastrophically. Although we show the results here only for the HS of the thermal accretion disk, it is clear that a similar analysis could be carried through for the corona HS. A mission like *LOFT* would thus make it possible to test the predictions of the HS in good detail. The high statistical accuracy of the data would even enable the parameters of the HS (e.g., its size) to be constrained.

The HS thermal emission (direct and reflected) is polarized to between ∼1% and ∼10% and exhibits large-amplitude polarization swings (see Table 1). According to our simulation, the HS contributes a fraction of $f \approx 9\%$ to the total emission; the HS model thus predicts that the overall polarization fraction varies by $\sim \pm f(\Pi_{\rm max} - \Pi_{\rm min})/2 \approx 0.4\%$ as a function of HS phase where Π is the polarization fraction. This prediction for HS in coronal emission with the higher f but the lower variation in polarization is 0.3%. A specific prediction of the HS model is an anticorrelation of the polarization fraction as a function of the HS flux. The variations in polarization fraction of the competing HFQPO models are most likely much smaller. In the resonance model (e.g., Abramowicz & Kluźniak 2001; Abramowicz et al. 2003), a perturbation excites oscillatory modes close to the ISCO. Petri (2008) models the HFQPOs of GRS 1915+105 by assuming that a spiral wave in the inner part of the accretion disk is in resonance with vertical epicyclic

Table 1
Polarization Properties of The Schwarzschild and Kerr BHs

Black Hole	Hotspot Min. Polarization Fraction	Hotspot Max. Polarization Fraction	Disk Polarization Fraction
Schwarzschild (spin = 0)	0.17%	8.4%	3.2%
Kerr (spin = 0.95)	0.21%	9.5%	1%

Table 2
Polarization Properties of Different HFQPO Models

Model	Reference	Average Polarization Fraction	Max. Range of Variation in Polarization Fraction
HS model	Schnittman & Bertschinger (2004)	4.86%	4.6%
Resonance model	Petri (2008)	0.78%	<0.1%
Torus model	Rezzolla et al. (2003)	2.97%	<0.1%

oscillations. In this model, the brightening disk portion is a ring segment rather than a more localized HS. The polarization of the emission from the bright ring segment will be more similar to that of the HS *averaging over all phases*. The averaging process reduced the expected polarization by a factor of a few. In the torus model (Rezzolla et al. 2003) HFQPOs are the result of p-mode (pressure mode) oscillations of an accretion torus orbiting the BH close to the ISCO. The model assumes a non-Keplerian, geometrically thick disk resembling a torus rather than a disk. The HFQPOs are thought to arise from hydrodynamic or magnetohydrodynamic instabilities (Rezzolla et al. 2003). The authors set an upper limit on the radius r_t of the torus of GRS 1915+105 of $r_t < 2.7\ r_g$ because in the absence of stabilizing magnetic fields a larger torus would be susceptible to non-axisymmetric perturbations. We estimated the polarization of the emission from such a torus by considering the emission from a ring at a radial coordinate of $r_t = 2.7\ r_g$. The ring is optically thick, and for simplicity we assume that its flux changes sinusoidally with a frequency equal to the HFQPO and a maximum flux exceeding the minimum flux by a factor of 5. The torus model predicts variations in polarization of $\ll 1\%$. Furthermore, the minute peaks of the polarization fraction are *in phase* with the brightness peaks. The results described in this paragraph are summarized in Table 2.

Could a next-generation space-borne X-ray polarimeter like *PolSTAR* (a space-borne version of the balloon-borne X-Calibur experiment (Beilicke et al. 2012, 2014; Guo et al. 2013) with excellent sensitivity in the 3–50 keV energy band), *PRAXyS* (*Polarimetry of Relativistic X-ray Sources*, Jahoda et al. 2015), *IXPE* (*Imaging X-ray Polarimetry Explorer*, Weisskopf et al. 2014), or *XIPE* (*X-ray Imaging Polarimetry Explorer*, Soffitta et al. 2013) detect the variation in polarization predicted by the HS model? We considered two methods to search for the variations in polarization: (i) the analysis of the Fourier-transformed Stokes parameters and derived quantities, and (ii) the analysis of the polarization fraction and angle as functions of QPO phase. We evaluated the first method based on the Stokes parameters I_i, Q_i, and U_i for each detected X-ray photon, as defined in Kislat et al. (2015). We calculated the polarization fraction π_k of the kth time bin with the standard equation: $\pi_k = \sqrt{\sum_{i_k} Q_{i_k}^2 + U_{i_k}^2} \Big/ \sum_{i_k} I_{i_k}$. However, the Fourier transform of π_k did not show pronounced peaks near the QPO frequency, indicating that quantities other than π_k should be used to search for quasi-periodic variations of the polarization fraction. The second method requires us to determine a phase for each individual detected event, enabling the determination of phase-binned polarization fractions and polarization angles. As the detection rate of first-generation polarimeters for GRS 1915+105 would be ~100 counts s^{-1}, they would detect less than one photon during each HFQPO cycle (and an even smaller fraction of HS photons). Such a low rate would not enable the assignment of a QPO phase. The study of the polarization properties of HFQPOs would thus require the concurrent operation of a first-generation X-ray polarimeter with a *LOFT*-type timing mission. The latter instrument would supply the information for phase-binning the data from the polarimeter mission. Whereas the systematic errors on measurements of absolute polarization fraction with a polarimeter like *PolSTAR* are of the order of 0.25%, the systematic errors on *short-term variations in polarization fraction* are much smaller. We conclude that the detection of the polarization signatures of HSs would be challenging but not entirely impossible.

In this paper we simulated the simple thermal disk and a wedge corona geometry with a HS to model spectral and polarization signatures of a HS. Other disk models such as ADAF can produce a very hot gas in the innermost region of the disk, making the HS with a temperature higher than 5 keV, which can produce seed photons that are already in high energy bands, with a moderate upscattering in the small coronal region (Schnittman 2006). Also it will be exciting to do similar studies based on GRMHD codes that evolve the accretion disk and a HS self-consistently.

The authors acknowledge NASA support under grant # NNX14AD19G. B.B. acknowledges fellowship support through the Graduate School of Arts & Sciences of Washington University in St. Louis. The authors thank A. Ingram and F. Kislat for valuable comments.

REFERENCES

Abramowicz, M. A., Karas, V., Kluzniak, W., Lee, W. H., & Rebusco, P. 2003, PASJ, 55, 467
Abramowicz, M. A., & Kluźniak, W. 2001, A&A, 374, L19
Abramowicz, M. A., & Kluźniak, W. 2003, GReGr, 35, 69
Bardeen, J. M., Press, W. H., & Teukolsky, S. A. 1972, ApJ, 178, 347
Beilicke, M., Baring, M. G., Barthelmy, S., et al. 2012, in AIP Conf. Ser. 1505 (Melville, NY: AIP), 805
Beilicke, M., Kislat, F., Zajczyk, A., et al. 2014, JAI, 3, 1440008
Bellazini, R., Costa, E., Matt, G., et al. 2010, X-ray Polarimetry: A New Window in Astrophysics (Cambridge: Cambridge Univ. Press)
Belloni, T., Soleri, P., Casella, P., Méndez, M., & Migliari, S. 2006, MNRAS, 369, 305
Bozzo, E., Stella, L., van der Klis, M., et al. 2014, arXiv:1312.1697
Broderick, A. E., & Loeb, A. 2005, MNRAS, 363, 353

Bursa, M. 2005, in RAGtime 6/7: Workshops on Black Holes and Neutron Stars, ed. S. Hledk & Z. Stuchlk (Opava, Czech Republic: Silesian Univ.), 39
Bursa, M., Abramowicz, M. A., Karas, V., & Kluźniak, W. 2004, ApJL, 617, L45
Chandrasekhar, S. 1960, Radiative Transfer (New York: Dover)
Davis, S. W., Blaes, O. M., Hirose, S., & Krolik, J. H. 2009, ApJ, 703, 569
Dexter, J., & Blaes, O. 2014, MNRAS, 438, 3352
Dove, J. B., Wilms, J., & Begelman, M. C. 1997, ApJ, 487, 747
Fender, R. P., Garrington, S. T., McKay, D. J., et al. 1999, MNRAS, 304, 865
Feroci, M., Stella, L., van der Klis, M., et al. 2012, ExA, 34, 415
Fukumura, K., & Kazanas, D. 2008, ApJ, 679, 1413
Guo, Q., Beilicke, M., Garson, A., et al. 2013, APh, 41, 63
Haardt, F., & Maraschi, L. 1991, ApJL, 380, L51
Ingram, A., Maccarone, T., Poutanen, J., & Krawczynski, H. 2015, ApJ, 807, 53
Ingram, A., & van der Klis, M. 2013, MNRAS, 434, 1476
Jahoda, K., Kouveliotou, C., Kallman, T. R. & Praxys Team 2015, AAS Meeting Abstracts, 225, 338.40
Kato, S. 2003, PASJ, 55, 801
Kislat, F., Clark, B., Beilicke, M., & Krawczynski, H. 2015, APh, 68, 45
Krawczynski, H. 2012, ApJ, 754, 133
Lei, F., Dean, A. J., & Hills, G. L. 1997, SSRv, 82, 309
Li, L.-X., Narayan, R., & McClintock, J. E. 2009, ApJ, 691, 847
Li, Z., & Bambi, C. 2014, PhRvD, 90, 024071
Markovic, D., & Lamb, F. K. 2000, arXiv:astro-ph/0009169
McClintock, J. E., & Remillard, R. A. 2003, arXiv:astro-ph/0306213
Merloni, A., Vietri, M., Stella, L., & Bini, D. 1999, MNRAS, 304, 155
Meszaros, P., Novick, R., Szentgyorgyi, A., et al. 1988, ApJ, 324, 1056
Noble, S. C., Krolik, J. H., & Hawley, J. F. 2009, ApJ, 692, 411
Novikov, I. D., & Thorne, K. S. 1973, in Black Holes (Les Astres Occlus), ed. C. Dewitt & B. Dewitt (London: Gordon and Breach), 343
Nowak, M. A., Wilms, J., & Dove, J. B. 2002, MNRAS, 332, 856
Page, D. N., & Thorne, K. S. 1974, ApJ, 191, 499
Penna, R. F., McKinney, J. C., Narayan, R., et al. 2010, MNRAS, 408, 752
Penna, R. F., Sadowski, A., & McKinney, J. C. 2012, MNRAS, 420, 684
Petri, J. 2008, Ap&SS, 318, 181
Psaltis, D. 2008, LRR, 11, 9
Remillard, R. A., & McClintock, J. E. 2006, ARA&A, 44, 49
Rezzolla, L., Yoshida, S., Maccarone, T. J., & Zanotti, O. 2003, MNRAS, 344, L37
Schnittman, J. D. 2005, ApJ, 621, 940
Schnittman, J. D. 2006, PhD thesis, MIT (arXiv:astro-ph/0601406v1)
Schnittman, J. D., & Bertschinger, E. 2004, ApJ, 606, 1098
Schnittman, J. D., & Krolik, J. H. 2009, ApJ, 701, 1175
Schnittman, J. D., & Krolik, J. H. 2010, ApJ, 712, 908
Soffitta, P., Barcons, X., Bellazzini, R., et al. 2013, ExA, 36, 523
Stella, L., & Vietri, M. 1998, ApJL, 492, L59
Stella, L., & Vietri, M. 1999, PhRvL, 82, 17
Suchy, S., Uter, P., Tenzer, C., et al. 2012, Proc. SPIE, 8443, 84435M
Tagger, M., & Varniere, P. 2006, ApJ, 652, 1457
Timmer, J., & Koenig, M. 1995, A&A, 300, 707
Tomsick, J. A., & Kaaret, P. 2001, ApJ, 548, 401
Vincent, F. H., Varniere, P., Méheut, H., et al. 2013, arXiv:1310.0918
Wagoner, R. V., Silbergleit, A. S., & Ortega-Rodríguez, M. 2001, ApJL, 559, L25
Weisskopf, M. C., Bellazzini, R., Costa, E., et al. 2014, in AAS/HEAD 14, 116.15
Zamaninasab, M., Eckart, A., Dovciak, M., et al. 2011, MNRAS, 413, 322
Zamaninasab, M., Eckart, A., Witzel, G., et al. 2010, A&A, 510, A3